

Nonreciprocal plasmons in one-dimensional carbon nanostructures

Received: 29 July 2025

Álvaro Rodríguez Echarri^{1,2}, F. Javier García de Abajo^{3,4} & Joel D. Cox^{5,6} 

Accepted: 10 December 2025

Published online: 30 December 2025

 Check for updates

The directional control of light in miniaturized plasmonic waveguides holds appealing possibilities for emerging nanophotonic technologies, but is hindered by the intrinsic reciprocal optical response of conventional plasmonic materials. While the ability of graphene to sustain large electrical currents shows promise for nonreciprocal plasmonics, studies have been limited to extended samples characterized by linear electrical dispersion. Here, we theoretically explore quantum finite-size and nonlocal effects in the nonreciprocal response of mesoscale plasmonic waveguides comprised of drift-biased graphene nanoribbons (GNRs) and carbon nanotubes (CNTs). Using atomistic simulation methods based on tight-binding electronic states and self-consistent quantum mean-field optical response, we reveal that a moderate electrical bias can appreciably break reciprocity for propagation of guided plasmon modes in GNRs and CNTs exhibiting electronic band gaps. The excitation by a nearby point dipole emitter and subsequent propagation of guided plasmon modes can thus be actively controlled by the applied current, which can further be leveraged to mediate nonlocal interactions of multiple emitters. Our results establish graphene nanostructures as a promising atomically thin platform for nonreciprocal nanophotonics.

Plasmon polaritons at metal-dielectric interfaces have been widely explored to control the flow of electromagnetic energy on nanometer length scales¹. Ordinarily, the directionality of light propagation in plasmonic materials is governed by Lorentz reciprocity, which ensures a symmetric response when the light source and detector are exchanged². However, nonreciprocal responses in plasmonics, where electromagnetic wave propagation differs depending on direction, enable important functionalities such as optical isolation^{3,4}, unidirectional waveguiding^{5–7}, and control of radiative heat flow^{8,9}.

Reciprocity can be broken by applying static magnetic fields¹⁰, where the enhanced light-matter interactions associated with plasmon resonances can boost the otherwise intrinsically low magneto-optical response of noble metals³. In an alternative approach, plasmon-driven nonlinear optical phenomena can trigger

nonreciprocal effects¹¹, although strategies for nonreciprocal photonics based on nonlinear optics present inherent limitations associated with unwanted backward-propagating noise^{12,13}. These constraints underscore the need for compact nanophotonic platforms that exhibit robust nonreciprocal behavior without relying on cumbersome magnetic biasing or power-intensive nonlinear optical processes^{8,14,15}.

Electrically doped graphene has emerged as a promising two-dimensional (2D) material platform for plasmonics, supporting plasmon resonances with high spatial dispersion that can be actively tuned by injecting charge carriers¹⁶. Beyond enabling active modulation of plasmon resonances through electrostatic gating, the ability of graphene to sustain ultrahigh current densities^{17–20} can be harnessed for nonreciprocal plasmonics, circumventing the use of large applied magnetic fields^{21–23}. Experimental studies of graphene

¹Max-Born-Institut, Berlin, Germany. ²Center for Nanophotonics, NWO Institute AMOLF, Amsterdam, The Netherlands. ³ICFO-Institut de Ciències Fotoniques, The Barcelona Institute of Science and Technology, Castelldefels (Barcelona), Spain. ⁴ICREA-Institució Catalana de Recerca i Estudis Avançats, Barcelona, Spain. ⁵POLIMA—Center for Polariton-driven Light–Matter Interactions, University of Southern Denmark, Odense M, Denmark. ⁶Danish Institute for Advanced Study, University of Southern Denmark, Odense M, Denmark. ✉e-mail: cox@mci.sdu.dk

subjected to applied direct currents have demonstrated that drifting charge carriers in the carbon monolayer can appreciably break the reciprocity of plasmon propagation along the direction of current flow^{24–26}.

Nonreciprocal plasmon polaritons in drift-biased graphene have been widely studied in a semiclassical electrodynamic framework, adopting nonlocal 2D conductivity models obtained by populating the conical electronic band structure of graphene with a skewed Fermi-Dirac distribution^{21–23,27} or by introducing a Doppler-shifted frequency in the local conductivity^{28–30}. In analogy to the Doppler shift, Fizeau shifts in the plasmon wavelength of drift-biased graphene have been experimentally measured using scanning near-field optical microscopy^{24,25}. In the presence of an applied direct current, graphene plasmons launched by localized light sources, such as point dipoles and energetic free electrons, are predicted to more efficiently transport optical energy in a preferential direction^{31–33}.

The patterning of graphene on nanometer length scales offers further possibilities to tailor plasmon resonances and engineer nanoscale light-matter interactions. In particular, one-dimensional (1D) carbon nanostructures, such as graphene nanoribbons (GNRs) and carbon nanotubes (CNTs), have been recognized as ideal candidates for plasmonic waveguiding that can be tuned passively by selecting the structure size or actively by modifying charge carrier doping levels^{34–39}. In the mesoscopic regime, quantum confinement effects in the electronic band structure of these systems can considerably impact not only their transport properties^{40–43}, but also the associated plasmonic response^{44–46}. These effects have yet to be explored in the dispersion of plasmon polariton modes supported by 1D carbon nanostructures with $\lesssim 10$ nm lateral size, with plasmons in GNRs and CNTs exhibiting high sensitivity to edge termination (armchair or zigzag) and structural chirality, respectively.

Here, we explore nonreciprocal plasmon polaritons in drift-biased GNRs and CNTs. Our analysis is based on an atomistic tight-binding description of carbon nanostructures that captures salient features in the electronic band structure due to edge termination in GNRs and structural chirality in CNTs. Nonlocal effects in the optical response of 1D carbon nanostructures to a point dipole excitation are incorporated in the framework of the random-phase approximation (RPA), employed here to resolve the dispersion of waveguided plasmons propagating along or against a drifting equilibrium electron distribution. Atomistic results predict a much greater dependence on drift current compared to estimates based on an electrodynamic description of analogous 1D carbon nanostructures, adopting a bulk 2D conductivity obtained from a semiclassical description of drift-biased graphene. In particular, topological effects in the electronic structure of zigzag GNRs and CNTs are shown to strongly impact the nonreciprocal response. Our results indicate that a strong imbalance of plasmon emission in opposite directions along these 1D carbon nanostructures, which can be controlled by the direction and magnitude of the applied currents, establishes these systems as a viable platform for active nonreciprocal nanophotonics.

Results

In what follows, we simulate the local density of optical states (LDOS) using atomistic and semiclassical descriptions of GNRs and CNTs under an applied drift bias. The LDOS at $\mathbf{r}_0 = (x_0, y_0, z_0)$ is characterized by the self-interaction of a point dipole with moment \mathbf{p} that oscillates with frequency ω , so we have $\text{LDOS} \propto \text{Im}\{\mathbf{p} \cdot \mathbf{E}^{\text{ind}}(\mathbf{r}_0, \omega)\}$, where \mathbf{E}^{ind} denotes the electric field produced by the nanostructure in response to the dipole at \mathbf{r}_0 . To study the nonreciprocal response of 1D systems characterized by translational invariance in the y -direction, we decompose the frequency-dependent field induced by the dipole as $\mathbf{E}^{\text{ind}}(\mathbf{r}_0, \omega) = (2\pi)^{-1} \int dq \vec{\mathcal{E}}_q(x_0, z_0, \omega) e^{iqy_0}$ in terms of spatial Fourier

components $\vec{\mathcal{E}}_q$, and define the wave-vector-resolved LDOS function¹

$$\mathcal{D}_q(x_0, z_0, \omega) = \frac{1}{2\pi^2 \omega |\mathbf{p}|^2} \text{Im}\left\{ \mathbf{p} \cdot \vec{\mathcal{E}}_q(x_0, z_0, \omega) \right\}. \quad (1)$$

The directional emission of a dipole near a GNR or CNT can then be quantified by defining a dissymmetry factor as

$$g = 2 \frac{\sum_{\pm} \int_0^{\pm\infty} dq \mathcal{D}_q}{\int_{-\infty}^{\infty} dq \mathcal{D}_q}, \quad (2)$$

which measures the relative difference of contributions to the LDOS from waves propagating with positive ($q > 0$) and negative ($q < 0$) wave vectors.

Graphene nanoribbons

We consider guided plasmon polaritons launched by a nearby point dipole source in drift-biased graphene nanoribbons (GNRs) with finite width W along $\hat{\mathbf{x}}$, lying in the $z = 0$ plane, and having exclusively armchair (AC) or zigzag (ZZ) edge terminations, as illustrated schematically in the upper and lower panels of Fig. 1a, respectively. In this scenario, guided plasmons that propagate along (against) the drift current parallel to $\hat{\mathbf{y}}$ are Doppler shifted to longer (shorter) wavelengths. Accordingly, the rate at which the dipole excites waveguided plasmons will exhibit a directional dependence. To explore this phenomenon, we calculate the LDOS in the framework of the RPA from the tight-binding (TB) electronic Bloch states of the considered AC and ZZ GNRs (see Methods). In Fig. 1b, we plot the energies $\hbar\epsilon_{j,k}$ of electronic bands indexed by j as a function of Bloch wave vector k in the direction of translational lattice symmetry for GNRs of width $W \approx 10$ nm (grey dots). Following the prescription that we introduce in Methods, the effect of drift currents induced by an in-plane electric field E^{DC} polarized along $\hat{\mathbf{y}}$ (the direction of translational invariance) is contained in the electronic occupation factors $f_{j,k}$ satisfying the steady-state limit of the Boltzmann transport equation,

$$\left(1 - \frac{e\tau}{\hbar} E^{\text{DC}} \frac{\partial}{\partial k} \right) f_{j,k} = f_{j,k}^{(0)}, \quad (3)$$

where τ is a phenomenological relaxation time introduced here to account for inelastic scattering and

$$f_{j,k}^{(0)} = \left[e^{(\hbar\epsilon_{j,k} - \mu)/k_B T} + 1 \right]^{-1} \quad (4)$$

are the occupation factors in the absence of any drift current, specified by the Fermi-Dirac distribution for a chemical potential μ and an electron temperature T . Within this framework, we specify the carrier relaxation time entering Eq. (3) through the relation $\tau = \mu^{\text{DC}} E_F / (ev_F^2)$ for extended graphene⁴⁷, where μ^{DC} is the DC electron mobility, E_F is the Fermi energy, and $v_F \approx c/300$ is the Fermi velocity. Unless otherwise specified, we use a conservative value for the electron mobility $\mu^{\text{DC}} = 500 \text{ cm}^2 \text{V}^{-1} \text{s}^{-1}$ throughout this work. In practice, Eq. (3) is solved for a discrete set of wave vectors k within the first Brillouin zone of each band by discretizing the differential operator and imposing periodic boundary conditions. For GNRs doped with additional charge carriers corresponding to $\mu = 0.5 \text{ eV}$ at room temperature $T = 300 \text{ K}$, such that states with energies $\hbar\epsilon_{j,k} \lesssim \mu$ (indicated by the orange shaded regions in Fig. 1b) are occupied when $E^{\text{DC}} = 0$, the drifting electron distribution induced by an applied field $E^{\text{DC}} = 5.2 \text{ MV m}^{-1}$ is indicated by the color of the electronic bands in Fig. 1b (see vertical colorbar). Notable asymmetry in the occupation factors appears around the Dirac points in drift-biased GNRs, resulting in a distinguishable optical response for fields with positive or negative in-plane optical momenta. In the Supporting Information (SI), we present calculations of the

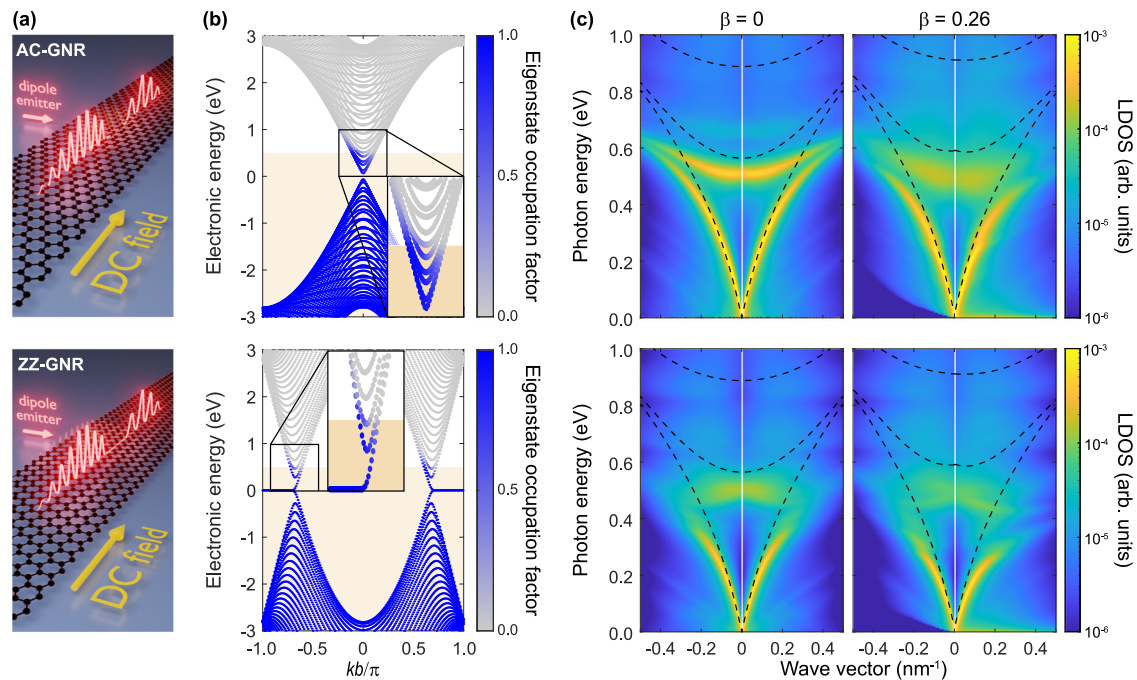


Fig. 1 | Nonreciprocal plasmons in drift-biased graphene nanoribbons. **a** Guided plasmon polaritons are launched by a point dipole emitter and propagate with different dispersion relative to the applied direct current (DC) in graphene nanoribbons (GNRs) with either armchair (AC, upper panel) or zigzag (ZZ, lower panel) edge terminations. **b** The one-dimensional electronic band structures of AC (upper panel) and ZZ (lower panel) GNRs of $W \approx 10$ nm width are plotted as functions of the Bloch wave vector k in the direction of lattice translational symmetry, normalized in each case to the respective GNR unit cell period b . In the absence of an applied DC field ($E^{\text{DC}} = 0$), the bands are occupied up to the Fermi energy

$E_F = 0.5$ eV (shaded orange region), while the occupation factors of GNRs for a static field of amplitude $E^{\text{DC}} = 5.2$ MV m^{-1} are indicated by the colors of the bands (see colorbar). **c** Wave-vector-resolved local photonic density of states (LDOS) for AC (upper panels) and ZZ (lower panels) GNRs obtained from atomistic simulations (contour plots) in the absence ($E^{\text{DC}} = 0$) and presence ($E^{\text{DC}} = 5.2$ MV m^{-1}) of an applied DC field, with corresponding plasmon dispersions predicted by the semi-classical electrodynamic model for the indicated drift velocities $v = \beta v_F$ (dashed curves).

electronic band structures and occupation factors of the considered $W \approx 10$ nm AC (Supplementary Fig. S1) and ZZ (Supplementary Fig. S2) GNRs under different configurations of charge carrier doping and applied field strength.

To explore the effects of drift current on the GNR plasmon dispersion, we simulate the LDOS in Fig. 1c for the $W \approx 10$ nm AC (upper panel) and ZZ (lower panel) GNRs, obtained in each case for a dipole polarized along \hat{x} and positioned in the GNR plane 5 nm away from the ribbon edge. Prominent features associated with guided plasmon polaritons appearing in the LDOS show that their dispersion is independent of propagation direction in the absence of a drift current (left panels). In general, the ZZ GNR exhibits a weaker plasmonic response due to the presence of zero-energy edge states in the electronic spectrum⁴⁴, while these modes also decay more rapidly with increasing wave vector due to Landau damping. We note, however, that edge disorder in fabricated structures may partially lift the degeneracy of these edge states, thereby mitigating their contribution to plasmon damping, although strong disorder would likely introduce additional scattering channels and further broaden the plasmon resonances. In the presence of a finite DC field, the drift current not only induces an asymmetry in the plasmon dispersion, but also damps the guided plasmon modes. Specifically, in both AC and ZZ GNRs, the low-energy monopole mode is diminished at high optical wave vectors and the dipolar GNR modes are generally quenched. Incidentally, the plasmon dispersion relations obtained from atomistic simulations are in reasonable agreement with the predictions based on a classical electrostatic model (see Methods), which are indicated in Fig. 1c by the dashed curves. To compare atomistic and classical models of drift-biased GNRs, we estimate the drift velocity $v = \beta v_F$ (expressed here in terms of the Fermi velocity $v_F \approx c/300$ in extended graphene) from $v = \mu^{\text{DC}} E^{\text{DC}}$. Additional details on the interdependence of the drift

velocity, electron mobility, and charge carrier doping level entering the classical model are presented in the SI (see Supplementary Fig. S3).

The nonreciprocal response of the drift-biased GNRs is quantified according to Eq. (2) by integrating the LDOS data shown in Fig. 1c over either exclusively positive ($q > 0$) or negative ($q < 0$) in-plane optical wave vectors. The resulting dissymmetry factors shown in Fig. 2a indicate a distinguishable response for AC (blue curve) and ZZ (red curve) GNRs predicted by atomistic simulations, reflecting the distinct plasmon dispersion relations shown in the LDOS plots of Fig. 1c, while the qualitative behavior of the emission into forward- and backward-propagating modes is captured by the classical simulations (dashed black curve) at higher energies. In Fig. 2b, we plot the dissymmetry factors g obtained when the dipole is instead oriented normally to the ribbon plane and centered 5 nm above the GNR (see inset), which, as shown in the SI, modifies the wave-vector-dependent coupling to waveguided plasmon modes predicted in atomistic (Supplementary Fig. S4) and classical (Supplementary Fig. S5) simulations, and thus also the spectral dependence of the corresponding dissymmetry factors. Qualitatively similar dissymmetry factors g are obtained at higher energies when the dipole is aligned with the ribbon and centered above it (Figs. S6), a configuration for which symmetry prohibits coupling of the lowest-order plasmon mode to the dipole. In Fig. 2c and d we show near-field maps of the electric field intensity $|\mathbf{E}|$ and the difference in amplitude $\Delta|\mathbf{E}| \equiv |\mathbf{E}(x, -y, z)| - |\mathbf{E}(x, y, z)|$ along the drift current direction in the plane 5 nm above the ZZ GNR under the conditions indicated in Fig. 2a and b, respectively. As shown in Supplementary Fig. S7 of the SI, this notable asymmetry can be more or less pronounced for different electric field components depending on the dipole position and orientation.

The nonreciprocal response of plasmons in drift-biased GNRs predicted in Figs. 1 and 2 above is based on a conservative estimate of

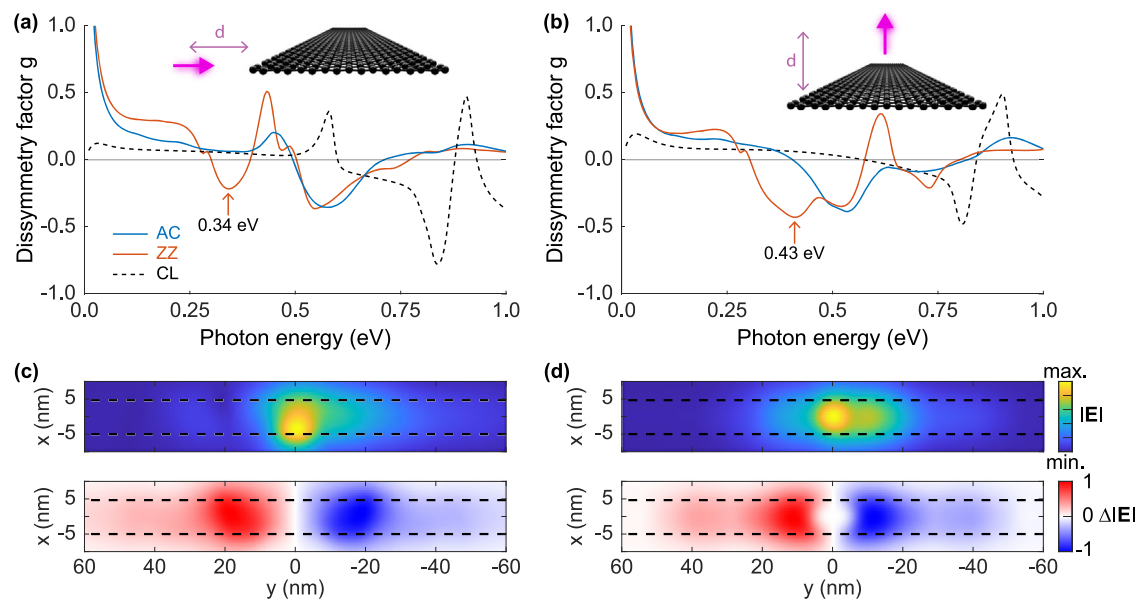


Fig. 2 | Dissymmetry of guided plasmon propagation in drift-biased graphene nanoribbons. The dissymmetry factor of Eq. (2) is calculated through atomistic simulations (solid curves) of the armchair (AC, blue curves) and zigzag (ZZ, red curves) edge-terminated graphene nanoribbons (GNRs) of $W \approx 10$ nm width considered in Fig. 1 for (a) a dipole oriented parallel to and placed in the GNR plane, at a distance $d = 5$ nm from the GNR edge, and (b) a dipole oriented normally to the

ribbon plane and centered $d = 5$ nm above the GNR (pink arrows indicate dipole positions and orientations). The dissymmetry factors predicted by semiclassical simulations of the same configurations are also shown (CL, dashed curves) (c, d) Maps of the electric field intensity $|E|$ and amplitude difference $\Delta|E| \equiv |E(x, -y, z)| - |E(x, y, z)|$ in the parallel plane 5 nm above the ZZ GNRs for the configurations shown in (a, b), respectively, at the photon energies indicated by the arrows in those panels.

the carrier mobility $\mu^{\text{DC}} = 500 \text{ cm}^2/(\text{V s})$, which accounts for scattering due to structural disorder and other inelastic processes that are inevitable in fabricated structures. Considerably higher values, on the order of $10^3 \text{ cm}^2\text{V}^{-1}\text{s}^{-1}$, can be obtained through chemical synthesis of GNRs⁴⁸, and further enhanced upon encapsulation in hexagonal boron nitride (hBN)⁴⁹. Such higher mobilities would further enhance the drift velocity attainable at a given bias field, therefore increasing the degree of plasmonic nonreciprocity, while also reducing plasmon damping. To effectively probe the asymmetry of guided polaritons, we have considered the self-interaction of dipoles near drift-biased GNRs. The dipole field amplitude decays approximately with the inverse of the distance, reducing the excitation efficiency of plasmon modes with enhanced dispersion leading to a larger nonreciprocal response. We have considered situations where dipoles are placed 5 nm away from the GNRs, a distance that is experimentally accessible in near-field spectroscopy and photoluminescence experiments employing quantum light sources.

Carbon nanotubes

The structural arrangement of carbon atoms in CNTs is characterized by indices (n, m) that define the tube type, with electronic structure varying from metallic to insulating. In Fig. 3, we simulate the plasmonic response of metallic (12,12), moderately semiconducting (20,0), and small-gap semiconducting (21,0) CNTs with diameters $D = (0.246 \text{ nm}/\pi)\sqrt{n^2 + m^2 + mn}$, which are all approximately $D \approx 1.6$ nm. Figure 3a illustrates the considered CNTs, which support guided polaritons that can be launched by a nearby point dipole source and may exhibit directional-dependent dispersion according to the applied DC field. In Fig. 3b, we present the electronic bands (curves) of the considered CNTs, uniformly populated up to a Fermi energy $E_F = 0.5$ eV in the absence of a drift current (shaded orange region), and occupied according to Eq. (3) (see colorbar) in the presence of a static field $E^{\text{DC}} = 5.2 \text{ MV m}^{-1}$. In the SI, we present the occupation factors of these CNTs under different carrier doping levels (see Supplementary Fig. S8). The wave-vector-resolved LDOS for a point dipole placed 5 nm away from the CNT centers is shown in Fig. 3c for unbiased (left) and

biased (right) CNTs, respectively, superimposing the classical dispersion (dashed curves) on the results obtained from atomistic simulations (contours).

The wave-vector-resolved LDOS in Fig. 3c indicates that the nonreciprocal plasmonic response of drift-biased CNTs is negligible for doped metallic and semimetallic CNTs, while the semiconducting drift-biased CNT exhibits a large nonreciprocal response, presumably due to the drastic difference in the available virtual electron-hole-pair excitations that configure the plasmon when the plasmon wave vectors are directed to the right or left sides (along or against the region of depletion in the electronic population of the conduction band). These conclusions are supported by the corresponding dissymmetry factors shown in Fig. 4a, while a more pronounced dissymmetry appears in the response of all considered CNTs at higher doping levels, when the noted difference in virtual excitations for right or left propagation are exacerbated. Figure 4b shows near-field maps of the electric field intensity and its difference produced by the (20,0) CNT, in the plane containing the dipole and oriented normally to it, at the photon energy 0.5 eV for which its dissymmetry is maximal.

Like GNRs, the nonreciprocal response of plasmons in CNTs (showcased in Figs. 3 and 4) is based on simulations adopting an electron mobility $\mu^{\text{DC}} = 500 \text{ cm}^2\text{V}^{-1}\text{s}^{-1}$. However, CNTs can exhibit much higher carrier mobilities, on the order of $\sim 10^4 \text{ cm}^2\text{V}^{-1}\text{s}^{-1}$, as their edge-free structure minimizes scattering from edge disorder that limits transport in narrow GNRs. High-quality CNTs with tailored electronic structure can be grown via chemical vapor deposition or by sorting chirality-selected tubes from bulk ensembles⁵¹. For representative drift fields of $E^{\text{DC}} \approx 5 \text{ MV m}^{-1}$ and device lengths on the order of a few micrometers, the corresponding voltages are well within the range of standard transport geometries. Directional plasmon propagation and Doppler-like shifts may be probed using scattering-type scanning near-field optical microscopy (s-SNOM), which has already been demonstrated on current-biased graphene systems^{24,25}, or by coupling to proximal optical emitters or nanoantennas to access the direction-dependent local density of optical states. Furthermore, pulsed or microwave biasing schemes can be

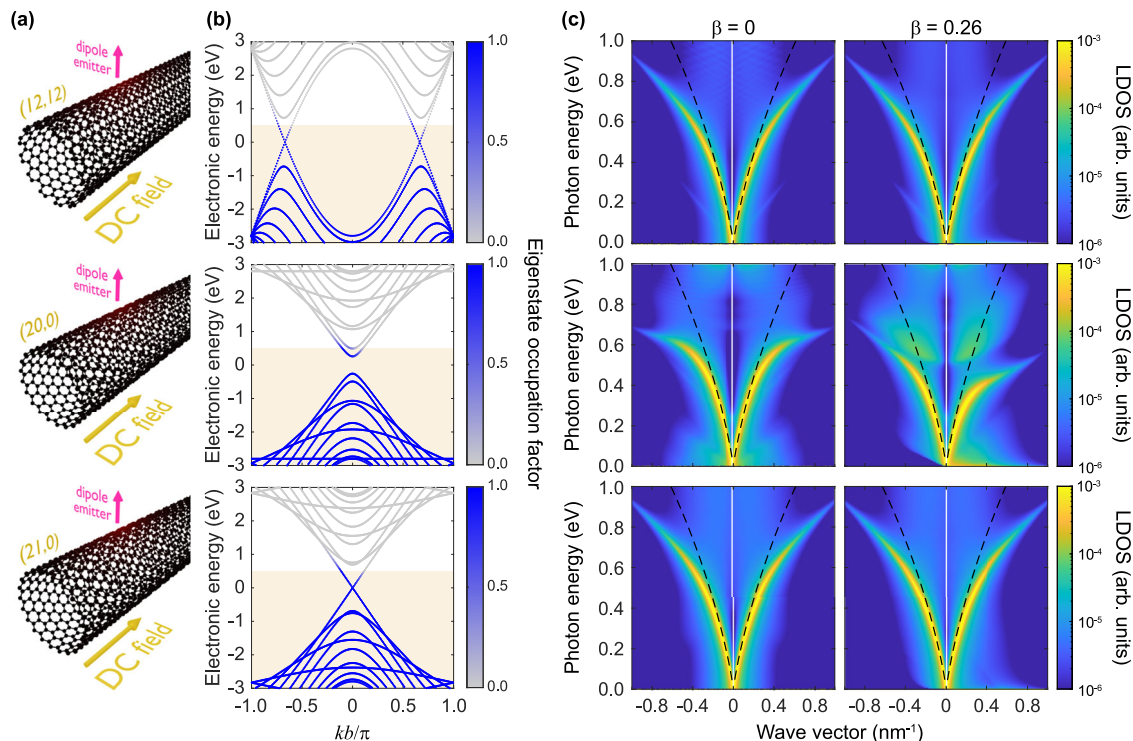


Fig. 3 | Nonreciprocal plasmons in drift-biased carbon nanotubes. **a** For CNTs with diameter $D \approx 1.6$ nm characterized by chiralities (12,12), (20, 0), and (21,0) in the upper, middle, and lower rows, respectively, we present schematic illustrations of the nanotubes interacting with a point dipole emitter. **b** Electronic band structure as a function of the Bloch wave vector k in the direction of translational invariance (grey curves), normalized in each case to the respective CNT unit cell period b , with the shaded orange region indicating fully occupied bands up to $E_F = 0.5$ eV doping in the absence of an applied DC field ($E^{DC} = 0$), while the

occupation factors for a static field of amplitude $E^{DC} = 5.2$ MV m^{-1} are indicated by the colors of the bands (see colorbar). **c** Wave-vector-resolved local photonic density of states (LDOS) obtained from atomistic simulations (contour plots) and presented along with the corresponding plasmon dispersion predicted from a classical electrodynamic model (dashed curves) are shown in the absence of a DC field (left column) and when applying a DC field with amplitude $E^{DC} = 5.2$ MV m^{-1} (right column). In all LDOS calculations, the dipole is considered to be oriented normally to and a distance $d = 5$ nm away from the tube axes.

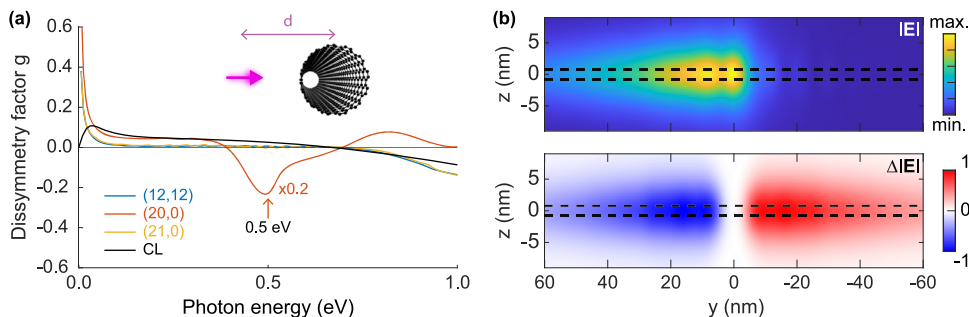


Fig. 4 | Dissymmetry factors for plasmons in drift-biased CNTs. **a** The dissymmetry factors for the (12,12), (20,0), and (21,0) electrically doped and drift-biased CNTs considered in Fig. 3 are plotted as blue, red, and yellow curves, respectively, under excitation by a dipole (indicated by the pink arrow) placed at a distance $d = 5$ nm away from the center and oriented along the radial direction

(see inset). The corresponding dissymmetry predicted from a classical model of a 1.6 nm diameter CNT (dashed curve) is shown for comparison. **b** Maps of the electric field intensity $|E|$ and amplitude difference $\Delta|E| \equiv |E(x, -y, z)| - |E(x, y, z)|$ for the (20,0) CNT in the plane normal to and containing the dipole at a photon energy of 0.5 eV indicated by the red arrow in (a).

employed to maintain a well-defined carrier drift during a fraction of the optical period, effectively mitigating Joule heating while preserving the nonreciprocal response. Taken together, these considerations demonstrate that the proposed effects are experimentally accessible using state-of-the-art material platforms and measurement techniques.

Dipole-dipole interaction

Nonreciprocal photonic environments offer appealing possibilities to manipulate nonlocal interactions between light scatterers, such as

nanoparticles or quantum light emitters (QEs). To explore this possibility in drift-biased carbon nanostructures, we consider the decay rate enhancement of a QE with dipole moment \mathbf{p}_1 placed at \mathbf{r}_1 due to the field produced by a second emitter with dipole moment \mathbf{p}_2 located at \mathbf{r}_2 . The dipole-dipole interaction is quantified by the coupling rate $\Gamma_{ij} = (2/\hbar) \int_{-\infty}^{\infty} dq \mathcal{D}_q^{(ij)}(x_j, z_j, \omega)$, where the analogous cross density of optical states (CDOS) function

$$\mathcal{D}_q^{(ij)} = \text{Im} \left\{ \mathbf{p}_i^* \cdot \vec{\mathcal{E}}_{i,q}(x_j, z_j, \omega) \right\} \tag{5}$$

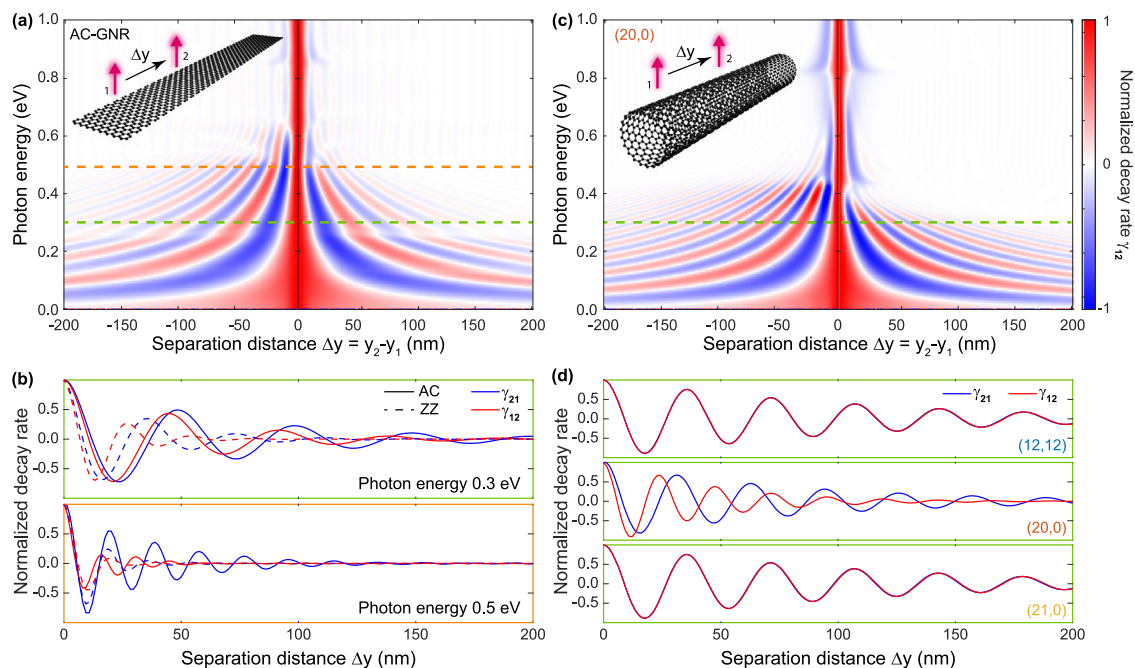


Fig. 5 | Dipole-dipole interactions mediated by nonreciprocal plasmons in 1D carbon nanostructures. **a** The normalized dipole-dipole interaction rate γ_{12} (associated with the field produced on dipole 1 at \mathbf{r}_1 by dipole 2 at \mathbf{r}_2) is plotted as a function of the dipole separation $\Delta y = y_2 - y_1$ along the GNR symmetry direction \hat{y} when both dipoles are centered 5 nm above and oriented normally to the drift-biased ($E^{\text{DC}} = 5.2 \text{ MV m}^{-1}$) $W \approx 10 \text{ nm}$ wide AC edge-terminated GNR (see inset). **b** The interaction rates γ_{21} (blue curves) and γ_{12} (red curves) for AC (solid curves) and ZZ (dashed curves) edge-terminated GNRs are shown for dipoles emitting at $\hbar\omega = 0.3 \text{ eV}$ (upper panel) and $\hbar\omega = 0.5 \text{ eV}$ (lower panel), at the photon energies

indicated in **(a)** by the dashed horizontal lines color-coordinated with the panel outlines in **(b)**. Panel **(c)** shows results analogous to those in **(a)** when the dipoles are oriented normally to and positioned 5 nm away from the axis of a (20,0) CNT, while **(d)** compares the directional dipole-dipole interaction rates of (12,12), (20,0), and (21,0) CNTs in the upper, middle, and lower panels, respectively, in analogy to **(b)** for GNRs, when the dipoles are emitting at $\hbar\omega = 0.3 \text{ eV}$, indicated by the horizontal dashed line in **(c)**. All results are shown for charge carrier doping levels corresponding to $E_F = 0.5 \text{ eV}$ in the absence of drift currents.

is expressed in terms of the Fourier components $\vec{\mathcal{E}}_{i,q}(x_j, z_j, \omega)$ of the electric field produced by \mathbf{p}_i at \mathbf{r}_j . Owing to the extreme field confinement of graphene plasmons, QEs can experience strongly enhanced spontaneous emission rates Γ_{ii}^{52} , while collective effects arising from plasmon-mediated interactions have been predicted to yield large inter-emitter coupling rates Γ_{ij} in nanoribbons³⁵ and nanodisks³³. Results for interacting emitters are presented in Fig. 5a, where we show the normalized decay rate³⁵

$$\gamma_{12} = \frac{\Gamma_{12}(\Delta y)}{\Gamma_{11}} \quad (6)$$

for two dipoles centered 5 nm above an AC edge-terminated GNR and separated by a distance $\Delta y = y_2 - y_1$ along the symmetry axis. The decay rate exhibits distinct behavior when the first dipole is placed in front ($\Delta y > 0$) or behind ($\Delta y < 0$) the second dipole (the drift current direction is set to $y > 0$). In analogy to the Doppler shift, the spatial oscillation of the dipole-dipole coupling, quantified by γ_{12} , exhibits a longer or shorter period depending on the relative positions of the dipoles and drift current flow direction. We explore this phenomenon in Fig. 5b, where the normalized decay rates computed for AC and ZZ GNRs are shown at the indicated photon energies, also highlighted by the color-coded horizontal dashed lines in Fig. 5a. The atomistic calculations reveal that the AC GNR enables stronger light-matter interaction than the ZZ edge-terminated GNR, resulting in a longer range of interaction as well as a larger dissymmetry in γ_{12} .

In Fig. 5c, d we explore nonreciprocal dipole-dipole coupling for CNTs. In analogy to the results for the AC edge-terminated GNR shown in Fig. 5a, we present the spatially resolved dipole-dipole interaction rate γ_{12} computed for the (20,0) CNT when the two interacting dipoles are each placed 5 nm away from the CNT axis and separated by a

distance $\Delta y = y_2 - y_1$ (see inset). The results for the (20,0) CNT are qualitatively similar to those obtained for the AC GNR. In Fig. 5d, we compare the nonreciprocal dipole-dipole interaction for dipoles oscillating at $\hbar\omega = 0.3 \text{ eV}$, for (12,12), (20,0), and (21,0) CNTs in the upper, middle (c.f. the horizontal dashed line in Fig. 5c), and lower panels. The (12,12) and (21,0) CNTs exhibit an almost fully reciprocal response, as anticipated from the minor effect of the applied drift current observed in the LDOS results of Fig. 3. In contrast, the moderately semi-conducting (20,0) drift-biased CNT exhibits a strong nonreciprocal plasmonic response, as indicated by comparing the dipole-dipole coupling rates γ_{12} and γ_{21} . Overall, the relative variations in the dipole-dipole interaction produced by nonreciprocal effects are substantial and can reach similar values as the dipole-dipole interaction in the reciprocal structures. The directionally biased plasmon modes provide a natural platform for tunable, nonreciprocal coupling between QEs and controlled emission pathways for quantum photonic applications.

Discussion

We have shown that drift currents in one-dimensional carbon nanostructures can induce a large nonreciprocal response that dramatically affects the propagation of guided plasmon polaritons on nanometer length scales. Our atomistic simulations indicate that the nonreciprocal plasmonic response is highly sensitive to features in the electronic band structure of GNRs and CNTs, where a particularly large asymmetry in the response can be induced due to the presence of electronic band gaps and topological features of their band structure. We further show that the nonlocal interaction between distant emitters can be manipulated by a drift current. The nonreciprocal plasmonic phenomena studied here depend crucially on the electron mobility μ^{DC} in GNRs and CNTs, a parameter related to the quality of the one-dimensional nanostructures that determines both the induced

drift current and the plasmon lifetimes. In our simulations we have adopted a conservative estimate for $\mu^{DC} = 500 \text{ cm}^2\text{V}^{-1}\text{s}^{-1}$, accounting for defects and other inelastic scattering mechanisms in fabricated structures. In practice, GNRs of $\sim 10 \text{ nm}$ width can be fabricated through bottom-up chemical synthesis—yielding atomically defined edges—or via top-down lithography followed by edge smoothing⁵⁴, while high-quality CNTs can be produced via chemical vapor deposition growth or by sorting chirality-selected tubes from bulk ensembles⁵¹. While the applied DC field strength used to establish the drift current is commensurate with that used in experiments, we envision that qualitatively similar effects can be produced by using microwave fields, such that a drift current with a well-defined direction is maintained during a fraction of the optical period in the nanosecond regime, enabling nonreciprocal optical responses over shorter times at infrared frequencies. The directional-dependent phase accumulation of guided plasmon modes in drift-biased CNTs and GNRs offers a versatile platform for nonreciprocal light-matter interactions, potentially enabling on-chip optical isolators and plasmonic diodes.

Methods

We develop models to describe the nonlocal optical response of drift-biased one-dimensional graphene nanostructures. We begin by deriving analytical expressions for the conductivity associated with free electrons in highly doped graphene, using the Boltzmann transport equation (BTE). We then outline a prescription to implement the nonlocal conductivity of drift-biased graphene in classical electrodynamic models for GNRs and CNTs. Classical models are contrasted with atomistic simulations of 1D graphene structures based on tight-binding electronic states and the RPA.

Conductivity of drift-biased graphene

We consider conduction electrons in a graphene sheet spanning the $\mathbf{R} = (x, y)$ plane, characterized by their parallel wave vector \mathbf{k} and energy $E_{\mathbf{k}} = \pm \hbar v_F |\mathbf{k}|$ for electron (upper sign) and hole (lower sign) doping. In the presence of a DC field \mathbf{E}^{DC} , the drifting of electrons at velocity \mathbf{v} can be described by a skewed Fermi-Dirac distribution⁵⁵

$$f_{\mathbf{k}}^{(0)} = \left[e^{(E_{\mathbf{k}} - \mu - \hbar \mathbf{v} \cdot \mathbf{k}) / k_B T} + 1 \right]^{-1}, \quad (7)$$

where μ is the chemical potential and T is the electronic temperature. The linear response to an applied optical field \mathbf{E} is then given in the BTE formalism as

$$\frac{\partial f_{\mathbf{k}}^{(1)}}{\partial t} \pm v_F \hat{\mathbf{k}} \cdot \nabla_{\mathbf{R}} f_{\mathbf{k}}^{(1)} - \gamma f_{\mathbf{k}}^{(1)} = -\frac{e}{\hbar} \mathbf{E} \cdot \nabla_{\mathbf{k}} f_{\mathbf{k}}^{(0)}, \quad (8)$$

from which the 2D current density is obtained as

$$\mathbf{J}(\mathbf{R}, t) = -\frac{e v_F g_s g_v}{4\pi^2} \int d^2 \mathbf{k} \hat{\mathbf{k}} f_{\mathbf{k}}^{(1)}(\mathbf{R}, t), \quad (9)$$

where $g_s = 2$ and $g_v = 2$ are spin and valley degeneracies, respectively. Decomposing the field and associated response functions in spatial and temporal Fourier components as $\mathbf{E}(\mathbf{R}, t) = \mathbf{E} e^{i(\mathbf{Q}\mathbf{R} - i\omega t)}$, the linear distribution becomes

$$f_{\mathbf{k}}^{(1)} = -\frac{ie}{\hbar} \frac{\nabla_{\mathbf{k}} f_{\mathbf{k}}^{(0)} \cdot \mathbf{E}}{\omega + i\gamma \mp v_F \hat{\mathbf{k}} \cdot \mathbf{Q}}, \quad (10)$$

which, after evaluating the gradient and inserting the result into Eq. (9), leads to the current

$$\mathbf{J} = \frac{ie^2 \mu_D}{\pi^2 \hbar^2} \int_0^{2\pi} d\varphi_{\mathbf{k}} \frac{v_F \hat{\mathbf{k}} (v_F \hat{\mathbf{k}} - \mathbf{v}) \cdot \mathbf{E}}{\omega + i\gamma \mp v_F \hat{\mathbf{k}} \cdot \mathbf{Q} (v_F - \mathbf{v} \cdot \mathbf{k})^2}. \quad (11)$$

Here, $\mu_D = \mu + 2k_B T \log(1 + e^{-\mu/k_B T})$ is a temperature-dependent Drude weight, and the angular integral is performed over all electron wave vector directions. The current in Eq. (11) implicitly defines the conductivity tensor σ through Ohm's law $\mathbf{J} = \sigma \cdot \mathbf{E}$.

In the specific case where the drift velocity $\mathbf{v} = \beta v_F \hat{\mathbf{v}}$ is parallel to the in-plane optical wave vector \mathbf{Q} , the anisotropic conductivity tensor elements for the electric field parallel (σ_{\parallel}) and perpendicular (σ_{\perp}) to the drift direction can be obtained analytically from Eq. (11) and Ohm's law as

$$\sigma_{\parallel}(\mathbf{Q}) = \frac{2\sigma_{\omega}}{(\alpha + \beta)^2} \left(\frac{1 + \alpha\beta}{\sqrt{1 - \alpha^2}} - \sqrt{1 - \beta^2} \right), \quad (12a)$$

$$\sigma_{\perp}(\mathbf{Q}) = \frac{2\sigma_{\omega}}{(\alpha + \beta)^2} \left(\frac{1 + \alpha\beta}{\sqrt{1 - \beta^2}} - \sqrt{1 - \alpha^2} \right), \quad (12b)$$

where $\sigma_{\omega} = ie^2 \mu_D / \pi \hbar^2 (\omega + i\gamma)$ is the local Drude conductivity of graphene and $\alpha = \mp v_F Q / (\omega + i\gamma)$. In what follows, we employ the above nonlocal conductivity of drift-biased graphene to perform classical electrodynamic calculations of GNRs and CNTs.

The temperature- and drift-dependent chemical potential $\mu(\beta)$ is determined by imposing conservation of electron population such that

$$N_e = 4 \sum_{\mathbf{k}} f_{\mathbf{k}}^{(0)}(\mu, \beta). \quad (13)$$

The chemical potential $\mu(\beta)$ depends on the bias electric DC field \mathbf{E}^{DC} , and N_e is fixed by imposing the condition $\mu = E_F$ when $\beta = 0$. The factor of 4 includes the spin and valley degeneracies (see Supplementary Fig. S4a in the SI).

Classical description of graphene nanoribbons (GNRs)

In the quasistatic approximation, the optical response of a 2D system to an external potential Φ^{ext} is characterized by the self-consistent scalar potential

$$\Phi(\mathbf{r}) = \Phi^{\text{ext}}(\mathbf{r}) + \frac{1}{\epsilon_{\text{eff}}} \int d^2 \mathbf{R}' \frac{\rho^{\text{ind}}(\mathbf{R}')}{|\mathbf{r} - \mathbf{R}'|}, \quad (14)$$

where the Coulomb interaction has been corrected with the average permittivity $\epsilon_{\text{eff}} \equiv (\epsilon_a + \epsilon_b)/2$ to account for the effect of screening by the homogeneous dielectric media above (ϵ_a) and below (ϵ_b) the 2D material, and $\rho^{\text{ind}}(\mathbf{R})$ is the induced 2D charge density in the material, placed in the $z = 0$ plane. Invoking the continuity equation $\rho^{\text{ind}} = - (i/\omega) \nabla \cdot \mathbf{J}$, Ohm's law $\mathbf{J} = \sigma \cdot \mathbf{E}$, and the electrostatic relation $\mathbf{E} = -\nabla \Phi$, the potential at points within the 2D material can be expressed self-consistently as

$$\left(1 - \frac{i}{\epsilon_{\text{eff}} \omega} \mathcal{M} \right) \Phi(\mathbf{R}) = \Phi^{\text{ext}}(\mathbf{R}), \quad (15)$$

where

$$\mathcal{M} \Phi(\mathbf{R}) = \int d^2 \mathbf{R}' \frac{1}{|\mathbf{R} - \mathbf{R}'|} \nabla_{\mathbf{R}'} \cdot [\sigma(\mathbf{R}') \cdot \nabla_{\mathbf{R}} \Phi(\mathbf{R}')] \quad (16)$$

is a linear integro-differential operator. Here, we are interested in studying the local photonic density of states in the vicinity of the 2D structure, characterized by the induced field generated by a point dipole \mathbf{p} at \mathbf{r}_0 acting back on itself, that is,

$$\mathbf{E}^{\text{ind}}(\mathbf{r}_0) = -\frac{1}{\epsilon_{\text{eff}}} \nabla_{\mathbf{r}_0} \int d^2 \mathbf{R}' \frac{\rho^{\text{ind}}(\mathbf{R}')}{|\mathbf{r}_0 - \mathbf{R}'|}, \quad (17)$$

where $\rho^{\text{ind}}(\mathbf{R}) = (i/\omega)\nabla_{\mathbf{R}} \cdot [\sigma(\mathbf{R}) \cdot \nabla_{\mathbf{R}}\Phi(\mathbf{R})]$ is the induced charge produced in the ribbon by the external potential $\Phi^{\text{ext}}(\mathbf{r}) = \epsilon_a^{-1} \mathbf{p} \cdot \nabla_{\mathbf{r}_0} |\mathbf{r} - \mathbf{r}_0|^{-1}$.

For a nanoribbon of finite width W along $\hat{\mathbf{x}}$ and infinite extension along $\hat{\mathbf{y}}$, the scalar potentials are conveniently decomposed in-plane waves with wave vector q as $\Phi(\mathbf{R}) = (2\pi)^{-1} \int dq \phi_q(x) e^{iqy}$, such that the spatial Fourier components satisfy the relation

$$\left(1 - \frac{i}{\epsilon_{\text{eff}}\omega} \mathcal{M}_q\right) \phi_q(x) = \phi_q^{\text{ext}}(x), \tag{18}$$

where we use the integro-differential operator

$$\begin{aligned} \mathcal{M}_q \phi_q(x) = & 2 \int dx' K_0(|q||x-x'|) \\ & \times \{ \partial_{x'} [\sigma_{\perp}(x') \partial_{x'} \phi_q(x')] - q^2 \sigma_{\parallel}(x') \phi_q(x') \} \end{aligned} \tag{19}$$

and

$$\phi_q^{\text{ext}}(x) = \frac{2}{\epsilon_a} \mathbf{p} \cdot \nabla_{\mathbf{r}_0} \left\{ K_0 \left[|q| \sqrt{(x-x_0)^2 + z_0^2} \right] e^{-iqy_0} \right\} \tag{20}$$

is the Fourier transform of the external potential. Following the prescription of refs. 56,57, Eq. (18) is solved by discretizing the spatial coordinate x in the ribbon domain defined through the conductivity as $\sigma(x) = f(x)\sigma(\omega)$, where $f(x)$ is a scalar function that is unity for points inside the ribbon and vanishes elsewhere, so that the potential can be obtained through matrix inversion. From Eq. (17), the induced field acting back on the dipole at \mathbf{r}_0 can then be found by evaluating

$$\mathbf{E}^{\text{ind}}(\mathbf{r}_0) = \int_{-\infty}^{\infty} \frac{dq}{2\pi} \vec{\epsilon}_q(\mathbf{r}_0) e^{iqy_0}, \tag{21}$$

where

$$\begin{aligned} \vec{\epsilon}_q(\mathbf{r}_0) = & -\frac{i}{\epsilon_{\text{eff}}\omega} \nabla_{\mathbf{r}_0} \int dx' K_0 \left[|q| \sqrt{(x_0-x')^2 + z_0^2} \right] \\ & \times \left\{ \partial_{x'} [\sigma_{\perp}(x') \partial_{x'} \phi_q(x')] - q^2 \sigma_{\parallel}(x') \phi_q(x') \right\} \end{aligned} \tag{22}$$

is the induced electric field decomposed in wave vectors q , which we use in Eq. (1) to compute the LDOS.

Classical description of carbon nanotubes (CNTs)

Following the procedure described in ref. 36, the induced electric field produced by a point dipole \mathbf{p} in the presence of a CNT of radius a can be written as

$$\mathbf{E}^{\text{ind}}(\mathbf{r}) = -\nabla_{\mathbf{r}} [(\mathbf{p} \cdot \nabla_{\mathbf{r}}) W^{\text{ind}}(\mathbf{r}, \mathbf{r}_0, \omega)]|_{\mathbf{r}_0=\mathbf{r}}, \tag{23}$$

where W^{ind} denotes the induced part of the total screened interaction $W(\mathbf{r}, \mathbf{r}_0) = |\mathbf{r} - \mathbf{r}_0|^{-1} + W^{\text{ind}}(\mathbf{r}, \mathbf{r}_0)$. The function W is defined as the electric scalar potential created at \mathbf{r} by an oscillating point charge $e^{-i\omega t}$ located at \mathbf{r}_0 , and is obtained by solving Poisson's equation. For \mathbf{r} and \mathbf{r}_0 both outside the cylindrical surface defined by the CNT, W^{ind} adopts the following analytical form:

$$\begin{aligned} W^{\text{ind}}(\mathbf{r}, \mathbf{r}_0, \omega) = & \frac{2}{\pi} \sum_{m=0}^{\infty} (2 - \delta_{m0}) \cos[m(\varphi - \varphi_0)] \\ & \times \int_{-\infty}^{\infty} dq r_m(q) e^{iq(z-z_0)} K_m(|q|\rho) K_m(|q|\rho_0), \end{aligned} \tag{24}$$

where

$$r_m(q) = -\frac{I_m^2(|q|a)\Delta}{K_m(|q|a)I_m(|q|a)\Delta + 1} \tag{25}$$

is a reflection coefficient expressed in terms of the quantity

$$\Delta(q) = \frac{4\pi i}{\omega a} \left[m^2 \sigma_{\perp}(q) + (qa)^2 \sigma_{\parallel}(q) \right]. \tag{26}$$

Using the screened interaction and taking the gradient of the potential, the wave-vector components of the induced electric field [see Eq. (21)] are found to be

$$\vec{\epsilon}_q(\mathbf{r}_0) = 2\hat{\rho} \sum_{m=0}^{\infty} (\delta_{m0} - 2) q^2 r_m(q) [K'_m(|q|\rho_0)]^2 \tag{27}$$

for a unit dipole oriented along the $\hat{\rho}$ direction and placed at the position of the dipole $\mathbf{r}_0 = (\rho_0, 0, 0)$. The above expression is used in Eq. (1) to compute the direction-dependent LDOS.

Atomistic description of one-dimensional carbon nanostructures

Following the approach of refs. 44,45, the electrons in carbon p_z orbitals $|l, m\rangle$ (located at the carbon atom positions \mathbf{R}_i in each unit cell m of a one-dimensional GNR or CNT) are described as Bloch states

$$|j, k\rangle = \frac{1}{\sqrt{M}} \sum_{l,m} a_{jl,k} e^{ikmb} |l, m\rangle. \tag{28}$$

Here, M denotes a (large) number of unit cells, k is the Bloch wave vector in the direction of translational lattice invariance, b is the unit cell period, and the coefficients $a_{jl,k}$ are determined by diagonalizing the tight-binding Hamiltonian $\mathcal{H}_{ll',k}^{\text{TB}}$ as

$$\sum_l \mathcal{H}_{ll',k}^{\text{TB}} a_{jl',k} = \hbar \epsilon_{j,k} a_{jl,k} \tag{29}$$

to yield the energies $\hbar \epsilon_{j,k}$ of electrons in each band j as a function of Bloch wave vector k in the direction of translational invariance.

In analogy to Eqs. (14) and (18), we write the spatial Fourier components of the self-consistent potential at site l produced in response to an external potential $\phi_{q,l}^{\text{ext}} e^{iqy}$ as

$$\phi_{q,l} = \phi_{q,l}^{\text{ext}} + \sum_{l'} v_{q,ll'} \rho_{q,l'}^{\text{ind}}, \tag{30}$$

where $v_{q,ll'} = \sum_m v_{l_0,l'm} e^{-iqmb}$ is the Fourier transform of $v_{l_0,l'm}$ (the spatial dependence of the Coulomb interaction between electrons in orbitals l and l' separated by m unit cells), and

$$\rho_{q,l}^{\text{ind}} = \sum_{l'} \chi_{q,ll'}^0 \phi_{q,l'} \tag{31}$$

is the induced charge, which, in the framework of the RPA, is expressed in terms of the noninteracting susceptibility

$$\begin{aligned} \chi_{q,ll'}^0 = & \frac{2e^2 b}{\hbar} \frac{1}{2\pi} \int_{-\pi/b}^{\pi/b} dk \sum_{jj'} (f_{j,k-q} - f_{j,k}) \\ & \times \frac{a_{jl,k} a_{j'l,k-q}^* a_{j'l',k}^* a_{j'l',k-q}}{\omega + i/(2\tau) - (\epsilon_{j,k} - \epsilon_{j',k-q})}, \end{aligned} \tag{32}$$

comprising a sum over electronic transitions weighted by occupation factors $f_{j,k}$.

In the absence of an applied DC field, the occupation factors entering Eq. (32) are determined by the Fermi-Dirac statistics,

that is,

$$f_{j,k} = f_{j,k}^{(0)} \equiv \left[e^{(h\varepsilon_{j,k} - \mu)/k_B T} + 1 \right]^{-1}. \quad (33)$$

To incorporate the applied DC field in atomistic calculations that capture the full one-dimensional multi-band electronic structure of GNRs and CNTs, we obtain $f_{j,k}$ by solving the Boltzmann transport equation [see Eq. (8)] in the static limit:

$$\left(1 - \frac{e\tau}{\hbar} E^{\text{DC}} \frac{\partial}{\partial k} \right) f_{j,k} = f_{j,k}^{(0)}, \quad (34)$$

which is the same as Eq. (3) in the main text. Note that the chemical potential is chosen to preserve the number of electrons [see Eq. (13)].

For a specified in-plane field E^{DC} oriented along the 1D structure, the electron drift velocity is estimated from $v = \mu^{\text{DC}} E^{\text{DC}}$, where μ^{DC} is the electron mobility, which dictates the mean-free path via the relaxation time⁴⁷

$$\tau = \frac{\mu^{\text{DC}} E_F}{ev_F^2} \quad (35)$$

and is related to the damping as $\gamma = \tau^{-1}$ (see Supplementary Fig. S4b in the SI for different choices of parameters). The above expressions thus relate the parameter $\beta = v/v_F$ entering the semiclassical calculations to the applied static field E^{DC} used in the TB-RPA formalism. In the SI, we study the electronic band structures of AC and ZZ GNRs in Figs. S5 and S6, respectively, as well as the occupation factors $f_{j,k}$ for different configurations of charge carrier doping and applied fields E^{DC} . Similarly, we show in Supplementary Fig. S7 the electronic bands for the CNTs of ≈ 1.6 nm diameter studied in this work.

Data availability

All data needed to evaluate the conclusions in the paper are present in the paper and the Supplementary Material. Additional data related to this paper may be requested from the authors.

Code availability

The formalisms described in the Methods provide a self-contained framework for implementing the semiclassical and atomistic calculations used in this study. The custom codebases used are not publicly available due to their complexity, but relevant code and information can be obtained from the corresponding author upon request.

References

- Hohenester, U. *Nano and Quantum Optics* (Springer, 2020).
- Potter, R. J. Reciprocity in optics. *Rep. Prog. Phys.* **67**, 717 (2004).
- Chin, J. Y. et al. Nonreciprocal plasmonics enables giant enhancement of thin-film Faraday rotation. *Nat. Commun.* **4**, 1599 (2013).
- Davoyan, A. & Engheta, N. Electrically controlled one-way photon flow in plasmonic nanostructures. *Nat. Commun.* **5**, 5250 (2014).
- Yu, Z., Veronis, G., Wang, Z. & Fan, S. One-way electromagnetic waveguide formed at the interface between a plasmonic metal under a static magnetic field and a photonic crystal. *Phys. Rev. Lett.* **100**, 023902 (2008).
- Bliokh, K. Y., Rodríguez-Fortuño, F. J., Bekshaev, A. Y., Kivshar, Y. S. & Nori, F. Electric-current-induced unidirectional propagation of surface plasmon-polaritons. *Opt. Lett.* **43**, 963 (2018).
- Li, S. et al. Unidirectional guided-wave-driven metasurfaces for arbitrary wavefront control. *Nat. Commun.* **15**, 5992 (2024).
- Hassani Gangaraj, S. A. & Monticone, F. Drifting electrons: non-reciprocal plasmonics and thermal photonics. *ACS Photonics* **9**, 806 (2022).
- Liu, T., Guo, C., Li, W. & Fan, S. Thermal photonics with broken symmetries. *ELight* **2**, 25 (2022).
- Jalas, D. et al. What is—and what is not—an optical isolator. *Nat. Photonics* **7**, 579 (2013).
- Boroviks, S., Kiselev, A., Achouri, K. & Martin, O. J. F. Demonstration of a plasmonic nonlinear pseudodiode. *Nano Lett.* **23**, 3362 (2023).
- Shi, Y., Yu, Z. & Fan, S. Limitations of nonlinear optical isolators due to dynamic reciprocity. *Nat. Photonics* **9**, 388 (2015).
- Mahmoud, A. M., Davoyan, A. R. & Engheta, N. All-passive non-reciprocal metastructure. *Nat. Commun.* **6**, 8359 (2015).
- Papaj, M. & Lewandowski, C. Plasmonic nonreciprocity driven by band hybridization in moiré materials. *Phys. Rev. Lett.* **125**, 066801 (2020).
- Monticone, F. et al. Nonlocality in photonic materials and metamaterials: roadmap. *Opt. Mater. Express* **15**, 1544 (2025).
- Gonçalves, P. A. D. & Peres, N. M. R. *An Introduction to Graphene Plasmonics* (World Scientific, 2016).
- Murali, R., Yang, Y., Brenner, K., Beck, T. & Meindl, J. D. Breakdown current density of graphene nanoribbons. *Appl. Phys. Lett.* **94**, 243114 (2009).
- Liao, L. et al. High-speed graphene transistors with a self-aligned nanowire gate. *Nature* **467**, 305 (2010).
- Son, S.-K. et al. Graphene hot-electron light bulb: incandescence from hbn-encapsulated graphene in air. *2D Mater.* **5**, 011006 (2017).
- Barajas-Aguilar, A. H. et al. Electrically driven amplification of terahertz acoustic waves in graphene. *Nat. Commun.* **15**, 2550 (2024).
- Sabbaghi, M., Lee, H.-W., Stauber, T. & Kim, K. S. Drift-induced modifications to the dynamical polarization of graphene. *Phys. Rev. B* **92**, 195429 (2015).
- Duppen, B. V., Tomadin, A., Grigorenko, A. N. & Polini, M. Current-induced birefringent absorption and non-reciprocal plasmons in graphene. *2D Mater.* **3**, 015011 (2016).
- Wenger, T., Viola, G., Kinaret, J., Fogelström, M. & Tassin, P. Current-controlled light scattering and asymmetric plasmon propagation in graphene. *Phys. Rev. B* **97**, 085419 (2018).
- Dong, Y. et al. Fizeau drag in graphene plasmonics. *Nature* **594**, 513 (2021).
- Zhao, W. et al. Efficient fizeau drag from dirac electrons in monolayer graphene. *Nature* **594**, 517 (2021).
- Dong, Y. et al. Current-driven nonequilibrium electrodynamics in graphene revealed by nano-infrared imaging. *Nat. Commun.* **16**, 3861 (2025).
- Blevins, M. G. & Boriskina, S. V. Plasmon fizeau drag in 3d dirac and weyl semimetals. *ACS Photonics* **11**, 537 (2024).
- Morgado, T. A. & Silveirinha, M. G. Negative landau damping in bilayer graphene. *Phys. Rev. Lett.* **119**, 133901 (2017).
- Morgado, T. A. & Silveirinha, M. G. Drift-induced unidirectional graphene plasmons. *ACS Photonics* **5**, 4253 (2018).
- Morgado, T. A. & Silveirinha, M. G. Nonlocal effects and enhanced nonreciprocity in current-driven graphene systems. *Phys. Rev. B* **102**, 075102 (2020).
- Correas-Serrano, D. & Gomez-Diaz, J. S. Nonreciprocal and collimated surface plasmons in drift-biased graphene metasurfaces. *Phys. Rev. B* **100**, 081410 (2019).
- Prudêncio, F. R. & Silveirinha, M. G. Asymmetric electron energy loss in drift-current biased graphene. *Plasmonics* **16**, 19 (2021).
- Morgado, T. A. & Silveirinha, M. G. Directional dependence of the plasmonic gain and nonreciprocity in drift-current biased graphene. *Nanophotonics* **11**, 4929 (2022).
- Christensen, J., Manjavacas, A., Thongrattanasiri, S., Koppens, F. H. L. & García de Abajo, F. J. Graphene plasmon waveguiding and

- hybridization in individual and paired nanoribbons. *ACS Nano* **6**, 431 (2012).
35. Huidobro, P. A., Nikitin, A. Y., González-Ballester, C., Martín-Moreno, L. & García-Vidal, F. J. Superradiance mediated by graphene surface plasmons. *Phys. Rev. B* **85**, 155438 (2012).
36. Martín-Moreno, L., García de Abajo, F. J. & García-Vidal, F. J. Ultraefficient coupling of a quantum emitter to the tunable guided plasmons of a carbon nanotube. *Phys. Rev. Lett.* **115**, 173601 (2015).
37. Lamata, I. S., Alonso-González, P., Hillenbrand, R. & Nikitin, A. Y. Plasmons in cylindrical 2d materials as a platform for nanophotonic circuits. *ACS Photonics* **2**, 280 (2015).
38. de Vega, S., Cox, J. D. & García de Abajo, F. J. Plasmons in doped finite carbon nanotubes and their interactions with fast electrons and quantum emitters. *Phys. Rev. B* **94**, 075447 (2016).
39. Calajó, G. et al. Nonlinear quantum logic with colliding graphene plasmons. *Phys. Rev. Res.* **5**, 013188 (2023).
40. Baringhaus, J. et al. Exceptional ballistic transport in epitaxial graphene nanoribbons. *Nature* **506**, 349 (2014).
41. Laird, E. A. et al. Quantum transport in carbon nanotubes. *Rev. Mod. Phys.* **87**, 703 (2015).
42. Wang, H. et al. Graphene nanoribbons for quantum electronics. *Nat. Rev. Phys.* **3**, 791 (2021).
43. Yao, X. et al. N=8 armchair graphene nanoribbons: solution synthesis and high charge carrier mobility. *Angew. Chem. Int. Ed.* **62**, e202312610 (2023).
44. Thongrattanasiri, S., Manjavacas, A. & García de Abajo, F. J. Quantum finite-size effects in graphene plasmons. *ACS Nano* **6**, 1766 (2012).
45. Cox, J. D., Silveiro, I. & García de Abajo, F. J. Quantum effects in the nonlinear response of graphene plasmons. *ACS Nano* **10**, 1995 (2016).
46. de Vega, S., Cox, J. D., Sols, F. & García de Abajo, F. J. Strong-field-driven dynamics and high-harmonic generation in interacting one dimensional systems. *Phys. Rev. Res.* **2**, 013313 (2020).
47. García de Abajo, F. J. Graphene plasmonics: challenges and opportunities. *ACS Photonics* **1**, 135 (2014).
48. Gu, Y., Qiu, Z. & Müllen, K. Nanographenes and graphene nanoribbons as multitailors of present and future materials science. *J. Am. Chem. Soc.* **144**, 11499 (2022).
49. Lyu, B. et al. Graphene nanoribbons grown in hbn stacks for high-performance electronics. *Nature* **628**, 758 (2024).
50. Dürkop, T., Getty, S. A., Cobas, E. & Fuhrer, M. S. Extraordinary mobility in semiconducting carbon nanotubes. *Nano Lett.* **4**, 35 (2004).
51. Yang, F. et al. Chirality pure carbon nanotubes: growth, sorting, and characterization. *Chem. Rev.* **120**, 2693 (2020).
52. Thanopoulos, I., Karanikolas, V. & Paspalakis, E. Strong coupling spontaneous emission interference near a graphene nanodisk. *Nanophotonics* **13**, 4545 (2024).
53. Iliopoulos, N., Thanopoulos, I., Paspalakis, E. & Karanikolas, V. Two-qubit entanglement dynamics under strong light-matter coupling near a graphene nanodisk. *Phys. Rev. A* **112**, 033720 (2025).
54. Saraswat, V., Jacobberger, R. M. & Arnold, M. S. Materials science challenges to graphene nanoribbon electronics. *ACS Nano* **15**, 3674 (2021).
55. Ashcroft, N. W. & Mermin, N. D. *Solid State Physics* (Harcourt College Publishers, 1976).
56. Christensen, T., Yan, W., Jauho, A.-P., Wubs, M. & Mortensen, N. A. Kerr nonlinearity and plasmonic bistability in graphene nanoribbons. *Phys. Rev. B* **92**, 121407 (2015).
57. Rasmussen, T. P., Rodríguez Echarrí, Á, García de Abajo, F. J. & Cox, J. D. Nonlocal and cascaded effects in nonlinear graphene nanoplasmonics. *Nanoscale* **15**, 3150 (2023).

Acknowledgements

We thank N. M. R. Peres for fruitful discussions. A.R.E. and F.J.G.A. acknowledge support from ERC (101141220-QUEFES) and the Spanish MICINN (Severo Ochoa CEX2019-000910-S). J.D.C. acknowledges support from Independent Research Fund Denmark (Grant No. 0165-00051B). The Center for Polariton-driven Light-Matter Interactions (POLIMA) is funded by the Danish National Research Foundation (Project No. DNRF165).

Author contributions

J.D.C. conceived the study. A.R.E., F.J.G.d.A., and J.D.C. developed the theory, discussed the results, and wrote the manuscript. A.R.E. performed the calculations, with input and analysis from J.D.C.

Competing interests

The authors declare no competing interests.

Additional information

Supplementary information The online version contains supplementary material available at <https://doi.org/10.1038/s41467-025-67872-5>.

Correspondence and requests for materials should be addressed to Joel D. Cox.

Peer review information *Nature Communications* thanks Xiaofei Xiao and the other, anonymous, reviewer(s) for their contribution to the peer review of this work. A peer review file is available.

Reprints and permissions information is available at <http://www.nature.com/reprints>

Publisher's note Springer Nature remains neutral with regard to jurisdictional claims in published maps and institutional affiliations.

Open Access This article is licensed under a Creative Commons Attribution-NonCommercial-NoDerivatives 4.0 International License, which permits any non-commercial use, sharing, distribution and reproduction in any medium or format, as long as you give appropriate credit to the original author(s) and the source, provide a link to the Creative Commons licence, and indicate if you modified the licensed material. You do not have permission under this licence to share adapted material derived from this article or parts of it. The images or other third party material in this article are included in the article's Creative Commons licence, unless indicated otherwise in a credit line to the material. If material is not included in the article's Creative Commons licence and your intended use is not permitted by statutory regulation or exceeds the permitted use, you will need to obtain permission directly from the copyright holder. To view a copy of this licence, visit <http://creativecommons.org/licenses/by-nc-nd/4.0/>.

© The Author(s) 2025